Available online at www.sciencedirect.com
ScienceDirect
Trans. Nonferrous Met. Soc. China 34(2024) 918−934
Transactions of Nonferrous Metals Society of China
www.tnmsc.cn

# Tailoring microstructure, mechanical and wear properties of $Mn_5Si_3$ reinforced Cu−35Zn−3Al alloy via melt superheat combined with pulsed magnetic field

Hang LI[1,2], Dong-tao NIU[1], Zhong-tao ZHANG[2], Fan YANG[1], Hong-xia WANG[1], Wei-li CHENG[1]

1. School of Materials Science and Engineering, Taiyuan University of Technology, Taiyuan 030024, China;
2. Golden Dragon Precise Copper Tube Group Inc, Chongqing 404100, China

Received 28 August 2022; accepted 28 February 2023

**Abstract:** The effects of melt superheat and pulsed magnetic field on the microstructure, mechanical and wear properties of the $Mn_5Si_3$ reinforced Cu−35Zn−3Al alloy were investigated. The results indicate that after the combined treatments, the hollow formation on the prism-shaped $Mn_5Si_3$ particles is inhibited, due to the enhanced solute migration in melt and promoted adsorption kinetics for crystal growth. The tensile strength and elongation of the forged alloy increase by 9.0% and 66.5%, respectively. The failure type of $Mn_5Si_3$ particles during tension transfers from brittle cleavage fracture to pulling out of the matrix due to the higher fracture strength with diminished stress concentration, which leads to enhanced reinforcement of matrix/particle load transfer. The wear resistance of alloy is significantly improved because of reduced delamination wear, since the severe shear fracture on the $Mn_5Si_3$ particles with hollows under friction induced plastic deformation is restrained, alleviating the subsurface originated crack propagation and spalling.

**Key words:** special brass; $Mn_5Si_3$ phase; pulsed magnetic field; strengthening mechanism; wear resistance

## 1 Introduction

Special brass is one kind of Cu−Zn based material with small additions of alloying elements such as Al, Mn, Si, Ni, and Sn. These additions play different roles, among which Al produces solid solution strengthening while Mn reacts with Si and forms the transition metal silicide of $Mn_5Si_3$ in the Cu−Zn system. $Mn_5Si_3$ has high thermal stability, high hardness and good anti-wear performance, and is commonly as reinforcement to endue brass alloys with high strength and excellent wear property at low cost [1]. Therefore, the $Mn_5Si_3$ reinforced brass is widely used to manufacture wear-resistant parts in the machine, automobile and aero industries, for instance synchronizer ring, self-lubricating bearing and piston hydraulic pump [2,3].

Due to the $D8_8$ hexagonal structure, $Mn_5Si_3$ phase tends to grow into hexagonal prism shape along a long axis in the brass alloys [4−6]. However, many studies have found that hollows easily appear in the center of prism-like $Mn_5Si_3$ particles. The hollow morphology combined with high brittleness of $Mn_5Si_3$ greatly increases its cracking tendency, seriously reducing both the strength and wear resistance of brass alloys [4−7]. LI et al [4] prepared the brass with different sizes of $Mn_5Si_3$ phase and indicated that the dimension of internal hollow rises with increasing the prism diameter. It is believed that during crystal growth, the melt region depleted of Mn and Si solutes is easy to generate in the prism center due to long diffusion distance, finally resulting in hollow formation inside

**Corresponding author:** Hang LI, Tel/Fax: +86-351-6010533, E-mail: lihang@tyut.edu.cn;
Wei-li CHENG, E-mail: chengweili7@126.com
DOI: 10.1016/S1003-6326(23)66443-X

the $Mn_5Si_3$ phase. BIE et al [5] investigated the morphology evolution of $Mn_5Si_3$ phase in the brass with various Mn contents. It was speculated that the impurities discharged from the grown $Mn_5Si_3$ are accumulated in the center of prism surface. Then, the restricted solute adsorption on the hexagonal plane leads to the presence of hollows in the prism center. Up to now, the formation mechanism of hollows on the $Mn_5Si_3$ phase has yet been clarified. Moreover, there is still a lack of effective means to control the hollow morphology of $Mn_5Si_3$ particles, so as to improve the mechanical and wear properties of brass alloys.

Melt superheat (MS) and pulsed magnetic field (PMF) have been successfully applied to improving the solidification structure of alloys. The MS treatment contributes to a uniform and disordered melt structure, promoting the homogeneous nucleation and growth of primary phases [8−10]. The PMF has dual effects of electromagnetic oscillation and stirring on the melt with introducing the forced convection. The application of PMF with appropriate intensity is able to reduce the temperature gradient and solute segregation in the melt, and a uniform structure with modified morphology of precipitated phase could be obtained [11−13].

Therefore, in this study the Cu−35Zn−3Al−2Mn−0.6Si alloy as a typical example was synthetically treated by MS and PMF to tailor the hollow morphology on the $Mn_5Si_3$ phase. Growth pattern and influential factors of $Mn_5Si_3$ phase, and the effect of $Mn_5Si_3$ morphology on the strength, ductility and wear resistance of the brass alloy are investigated. This work could have a great signification for tailoring the morphology of transition metal silicides to enhance performances of composite or alloy.

## 2 Experimental

### 2.1 Material and microstructure characterization

The studied alloy was prepared from pure Cu, Zn, Al, Ni, Sn and Pb, Cu−Mn and Cu−Si master alloys. The raw materials were melted in a graphite crucible using a medium-frequency induction furnace. For the combined treatments of MS and PMF, the well-mixed melt was first superheated to 1200 °C for 30 min and slowly cooled to 1000 °C. Then, the crucible was placed in the experimental setup with PMF triggered simultaneously, as shown in Fig. 1. The PMF was applied until the solidification process was ended. The input voltage and frequency were 700 V and 10 Hz, respectively, while the peak current was measured as about 500 A with pulse duration of 2 ms (Fig. 2(a)). For comparison, another alloy was cast without any treatment. The prepared cast ingots were 40 mm in diameter and 80 mm in height. After that the ingots were heated to 700 °C for 30 min and subsequently forged into circular plates with a deformation rate of 90%. The complete process route is shown in Fig. 2(b). Chemical compositions of the forged alloys measured by X-ray fluorescence (XRF, Shimadzu XRF1800) are presented in Table 1. For the convenience of discussion, two alloys without and with MS-PMF treatment are termed as T0 and T1, respectively. The phase composition of alloys was analyzed using an X-ray diffractometer (XRD,

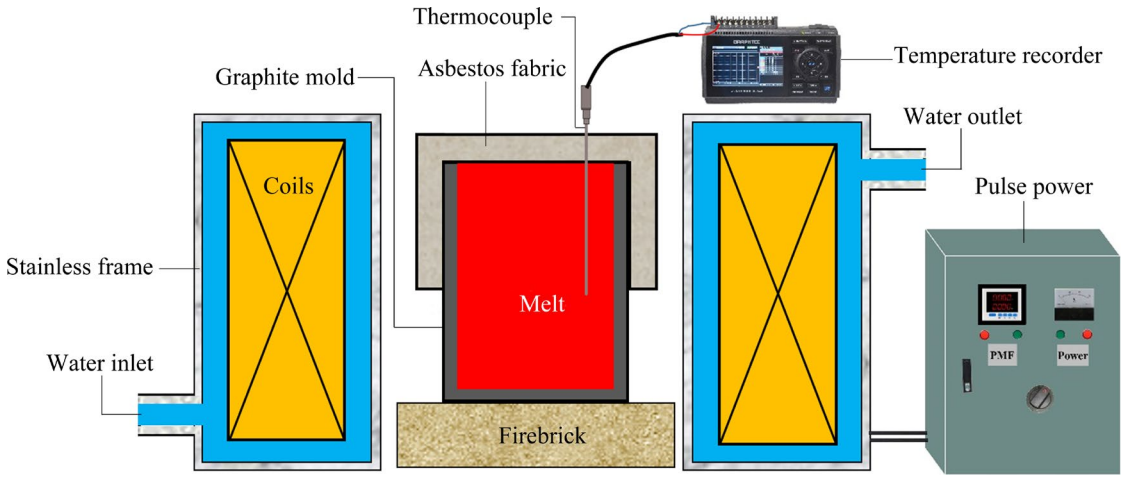


**Fig. 1** Schematic diagram of experimental setup

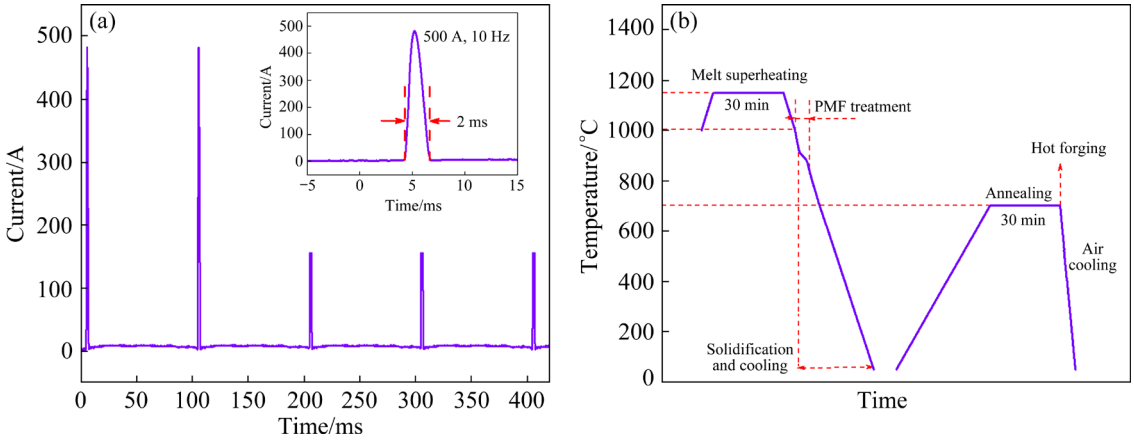


**Fig. 2** Current waveform through induction coil of PMF (a) and solidification and processing route of alloy (b)

**Table 1** Chemical composition of experimental alloys (wt.%)

| Condition | Alloy | Zn | Al | Mn | Si | Ni | Sn | Pb | Cu |
|---|---|---|---|---|---|---|---|---|---|
| Without treatment | T0 | 35.64 | 2.92 | 2.08 | 0.63 | 0.22 | 0.15 | 0.16 | Bal. |
| MS-PMF treatment | T1 | 35.47 | 2.89 | 2.11 | 0.61 | 0.21 | 0.15 | 0.14 | Bal. |

Rigaku Ultima TV). A scanning electron microscope (SEM, Mira 3XMU) and a transmission electron microscope (TEM, JEOL JEM-F200) were used to analyze the microstructures.

### 2.2 Tensile test

The tensile test was carried out using a universal tensile testing machine at room temperature at a strain rate of 0.5 mm/min. At least three tensile specimens with a size of 20 mm × 5 mm × 2 mm prepared from the same positions of forged samples, were measured for each condition.

### 2.3 Wear behavior

To characterize the wear resistance of brass alloys, dry sliding wear tests were carried out using a universal pin-on-ring configuration. The alloy pins, machined from the same positions of forged specimens, rotated along the vertical axis while rubbing against the ring made of quenched 0.45 wt.% C steel. The pin sample has a dimension of 4.8 mm in diameter and 12.7 mm in length, with one end of a hemispherical tip and a surface roughness of 0.2 μm. The total sliding distance is set to be 1000 m with a sliding speed of 0.5 m/s and an applied load of 180 N. Friction coefficient during the test was recorded by computer in real time. Mass loss of wear samples at different sliding distances was measured using an analytical balance with an accuracy of 0.1 mg. Before each weighing the samples were ultrasonically cleaned in an acetone bath and air dried.

The topography of worn surfaces for the pins and counterpart rings, as well as the morphology of wear debris, were characterized by SEM. The 3D morphology and depth profiles of worn surfaces of the pin samples were examined using a laser scanning confocal microscope (LSCM, OSL4000). The samples were also longitudinally sectioned and the microstructures below the wear surfaces were investigated.

## 3 Results and discussion

### 3.1 Microstructure and growth morphology of $Mn_5Si_3$ phase

Figure 3(a) shows the XRD patterns of alloys without and with MS-PMF treatment. It can be found that the main component is $\beta$ phase (bcc structure, solid solution based on electron compound CuZn). The formation of $Mn_5Si_3$ phase can be confirmed by the small diffraction peaks as shown in the partially enlarged patterns (Fig. 3(b)). The microstructures of as-cast alloys are displayed in Figs. 4(a, b). The gray matrix is $\beta$ phase and the particles distribute both within the grains and at the grain boundaries. According to the 3D morphology observation with EDS analysis after deep etching,

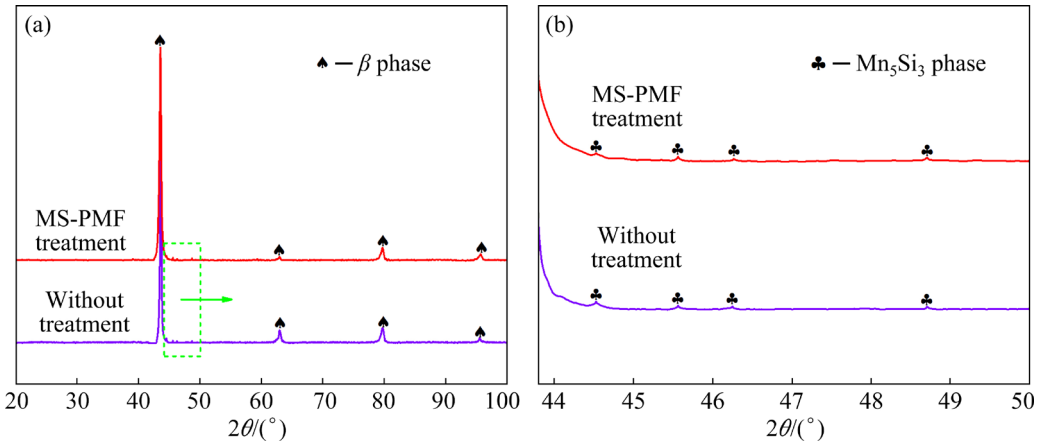


**Fig. 3** XRD patterns (a) and partial enlargement (b) of alloys without and with MS-PMF treatment

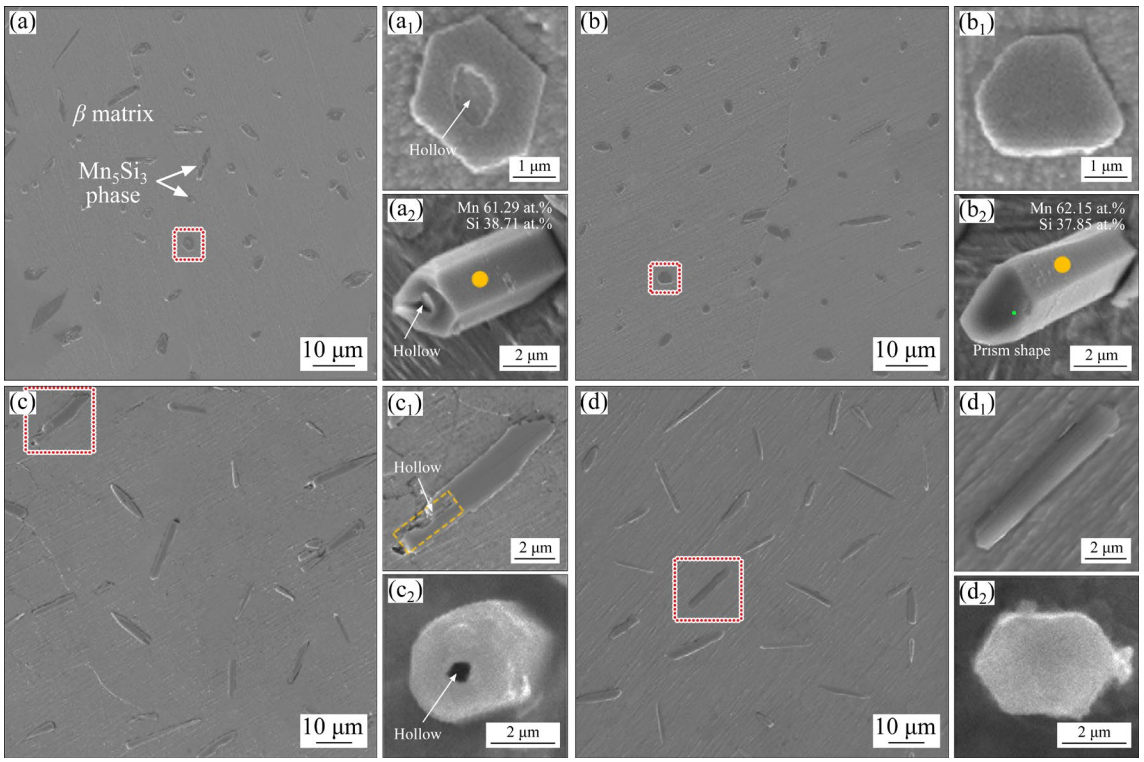


**Fig. 4** SEM images of alloys without and with MS-PMF treatment: (a, b) As-cast alloy; (c, d) Cross section of as-forged alloy; (a, c) T0; (b, d) T1; ($a_1$−$d_1$) Local magnification of $Mn_5Si_3$ particle in dot frame; ($a_2$−$d_2$) 3D morphology of $Mn_5Si_3$ particle

the particles are further proven to be $Mn_5Si_3$ and present the shape of long hexagonal prism. For the T0 alloy, the prism diameter is about 2.0 μm. The hollows can be clearly found in the center of particles via local magnification of microstructure (Fig. 4($a_1$)) and 3D morphology observation (Fig. 4($a_2$)). With the MS-PMF treatment, the dimension and distribution of particles present small variation and the hollows on the particles of the T1 alloy disappear. After the forging deformation, the particles turn to arrange along the circular plane and there is no obvious change in particle morphology, as shown in Figs. 4(c, d).

To investigate the crystal structure features of $Mn_5Si_3$ phase, the bright field TEM images and selected area electron diffraction (SAED) patterns for different crystal planes of $Mn_5Si_3$ particles are shown in Figs. 5(a−d). The results indicated that the prism side plane and hexagonal plane correspond to $(10\bar{1}0)$ and (0002) faces, respectively. The prism

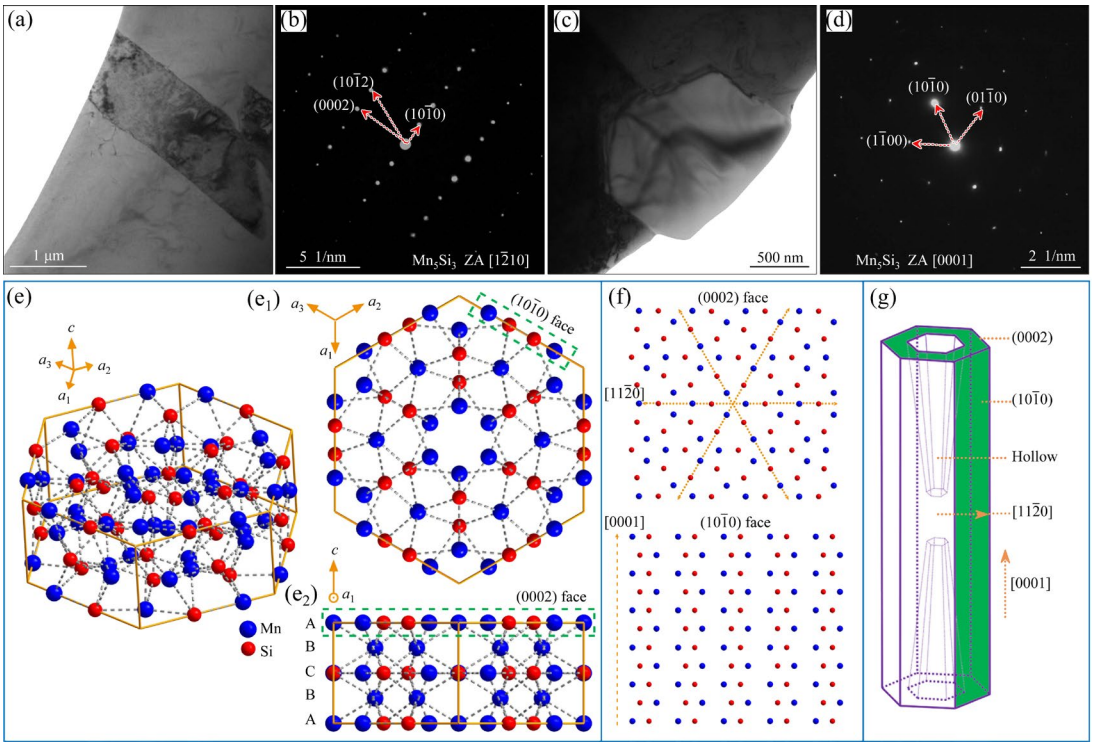


**Fig. 5** TEM images and crystal growth analysis for $Mn_5Si_3$ phase: (a, c) Bright field images; (b, d) SAED patterns; (e, $e_1$, $e_2$) Crystal structure and side views; (f) Atomic distribution of close-packed faces; (g) Schematic illustration of growth pattern

height is parallel to the [0001] orientation, namely the preferred growth direction of $Mn_5Si_3$ phase. The crystalline structure of $Mn_5Si_3$ is detailly analyzed as shown in Figs. 5(e, f), since it is an internal factor determining the final growth morphology [14]. $Mn_5Si_3$ has a $D8_8$ hexagonal structure with the space group of $P6_3/mcm$ and the lattice constants of $a$=0.691 nm, and $c$=0.481 nm [15]. The unit cell is composed of three different atomic planes with a stacking sequence of ABCBA, and atomic plane C can be obtained by rotating plane A with 180° (Fig. 5(e)). The positions and atomic distributions of close-packed faces (0002) and (10 $\bar{1}$ 0) are displayed in Figs. 5($e_1$, $e_2$, f). According to the Bravais-Friedel law, after crystal growth the close-packed faces are easily preserved owing to the lower surface energy [16]. In the theory of classical crystal growth, the crystal with lattice parameter $a \approx b > c$ tends to grow into elongated prismatic shape [14]. For this reason, $Mn_5Si_3$ grows the fastest along the $c$-axis, that is, ⟨0001⟩ direction. The hollow defects on the hexagonal face reduce its atomic density and also increase the growth rate along the ⟨0001⟩ direction. For other directions normal to $c$-axis, the growth rate oriented ⟨11$\bar{2}$0⟩ is faster due to complete arrangement of the Mn−Si periodic chains and thereby the {11$\bar{2}$0} faces would disappear during crystal growth. The {10$\bar{1}$0} faces have higher atomic density and slower attachment kinetics. The growth rate along the ⟨10$\bar{1}$0⟩ direction is lower and {10$\bar{1}$0} face can be eventually exposed on the surface. Combined with the typical faceted growth pattern, $Mn_5Si_3$ will grow into the shape of a long hexagonal prism after crystal growth. The indices of crystal planes and directions of hexagonal prism are present in Fig. 5(g), which are consistent with the TEM results.

### 3.2 Formation and control mechanism of hollow morphology on $Mn_5Si_3$ phase

The hollows in the center of $Mn_5Si_3$ particles should be formed under the influence of the external environment during the growth process. Given that the solute concentration and solute transfer are important environmental factors, to reveal the formation mechanism of internal hollows on the $Mn_5Si_3$ prism, the distribution of Mn and Si solutes in the center and surrounding areas of $Mn_5Si_3$ phase is investigated for the T0 alloy, as shown in Figs. 6(a−c). EDS analysis of Spots *A* and

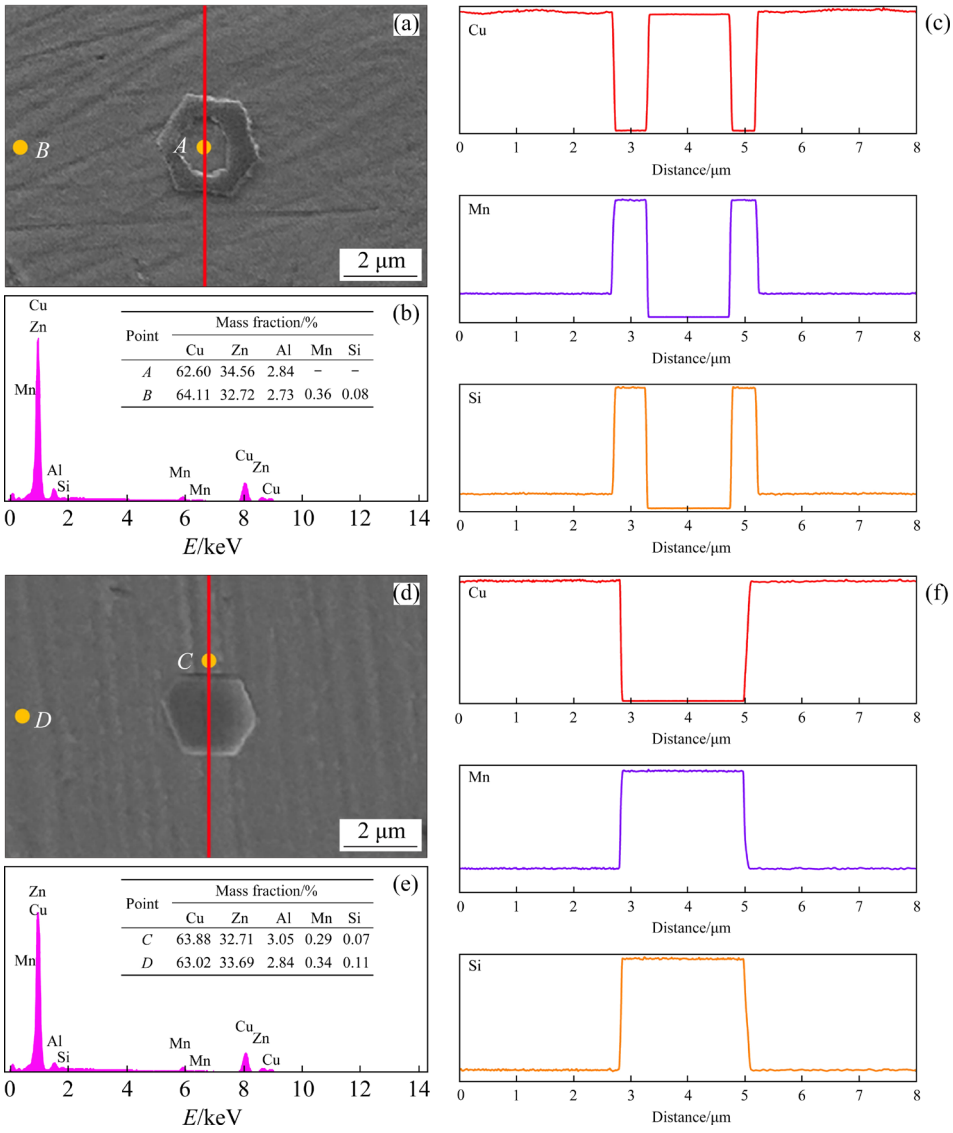


**Fig. 6** SEM images of $Mn_5Si_3$ particle with or without hollow in T0 alloy (a) and T1 alloy (d); (b, e) EDS results for spots in (a) and (d), respectively; (c, f) EDS line scan profiles of Cu, Mn and Si along red lines in (a) and (d), respectively

*B* in Fig. 6(a) indicates that a small amount of Mn and Si elements failing to react completely is dissolved in the $\beta$ matrix, while no Mn and Si are detected in the hollow area of $Mn_5Si_3$ phase. EDS line scan results further prove that the $\beta$ phase at entire hollow location forms the solute-depleted region of Mn and Si. In comparison, the distribution of Mn and Si solutes around $Mn_5Si_3$ phase in the T1 alloy becomes relatively uniform (Figs. 6(d−f)). The schematic illustration of hollow formation on the $Mn_5Si_3$ phase is displayed in Fig. 7(a). With the prism growth, Mn and Si atoms in melt are continuously adsorbed to the lattice sites of crystal faces, so that the solute concentration at the interface front decreases and the solute diffusion from surrounding melt is required to maintain the facet growth. Hence, with the increase of prism diameter, the melt region depleted of Mn and Si solutes tends to be generated in the prism center, due to the longer diffusion distance and barrier effect of the prism side planes. Then, the internal hollows will be left on the $Mn_5Si_3$ prism after crystal growth.

With the MS-PMF treatment, the $Mn_5Si_3$ phase grows into the morphology of a complete hexagonal prism in the T1 alloy, which should be ascribed to the promoted solute adsorption kinetics. In the favor of melt superheat, the distribution of Mn and Si solutes in melt becomes uniform and the dimension of solute atom clusters decreases, which benefits the homogeneous precipitation and grow-up of $Mn_5Si_3$ phase. Under the effect of periodically

changing PMF, an induced current is produced in the melt in turn. The melt will be subjected to a Lorentz force caused by the interaction of magnetic field and induced current, which can be explained as follows [17]:

$$F=J\times B \quad (1)$$

where $J$ is the induced current density, and $B$ is the magnetic flux density. The fields of Lorentz force and fluid flow under PMF were simulated using the commercial Ansys software. Figure 8(a) shows the calculated Lorentz force distribution in melt in one period of PMF, which demonstrates the simultaneous generation of electromagnetic oscillating and stirring. Figure 8(b) displays the time-averaged flow velocity distribution in melt under PMF. Fluid regions with different flow velocities can be observed, indicating the formation of effective forced convection, and the specific convection direction is shown in Fig. 8(c). Through the enhanced fluid movement, the ambient melt rich in Mn and Si solutes is able to migrate to the growth front of $Mn_5Si_3$ phase, resulting in the sufficient solute adsorption on the prism planes during crystal growth (Fig. 7(b)). Therefore, after the MS-PMF treatment, the $Mn_5Si_3$ phase eventually grows into the hexagonal prism-like morphology without center hollows.

### 3.3 Effect of $Mn_5Si_3$ morphology on mechanical properties

Figure 9 shows the typical engineering stress–strain curves and mechanical properties of forged alloys under different treatments. The ultimate tensile strength and elongation to fracture of the T0 alloy are 601 MPa and 9.2 %, respectively. After the MS-PMF treatment, the T1 alloy achieves high tensile strength of 655 MPa and high elongation of 15.3%, with increments of 9.0% and 66.3%, respectively. SEM images of fracture surfaces of the tensile samples are displayed in Fig. 10. For the T0 alloy, the tearing edges, small cleavage planes

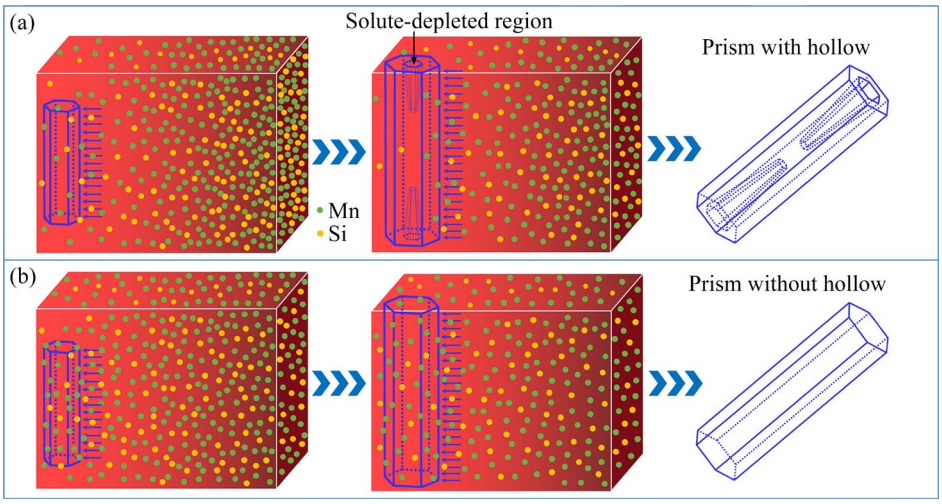


**Fig. 7** Schematic illustration of hollow formation and inhibition during $Mn_5Si_3$ growth under different treatments: (a) T0 alloy; (b) T1 alloy

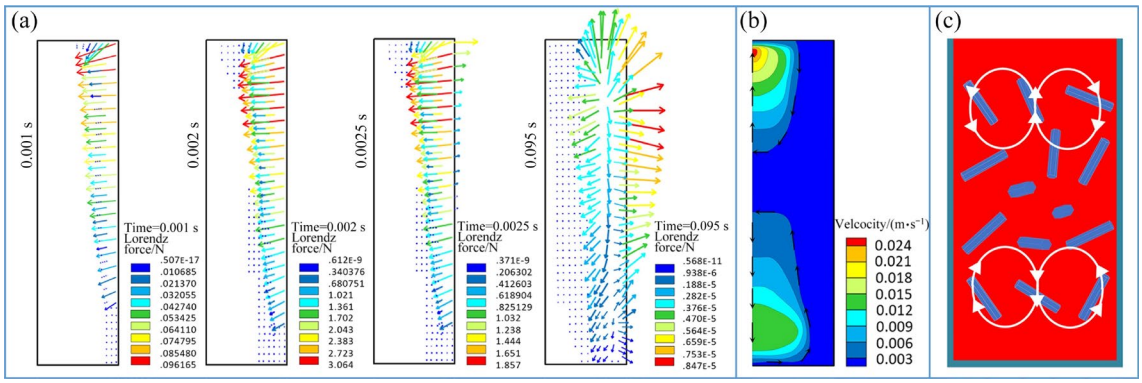


**Fig. 8** Lorentz force distribution in melt in one period of PMF (a), flow velocity distribution in melt under PMF (b), and schematic diagram of forced convection under PMF (c)

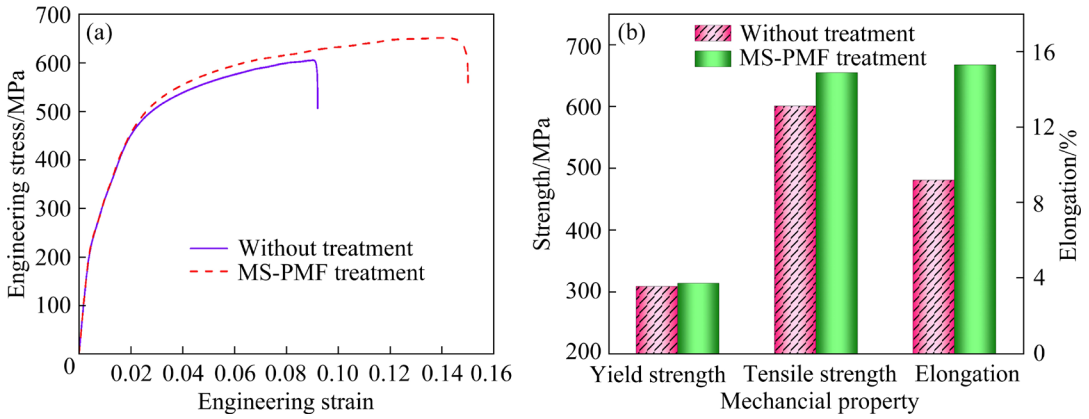


**Fig. 9** Engineering stress–strain curves (a) and mechanical properties (b) of alloys without and with MS-PMF treatment

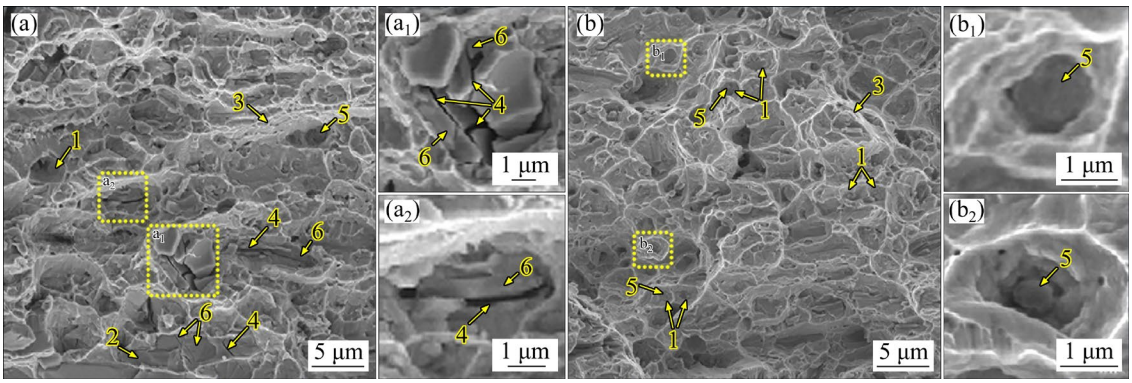


**Fig. 10** SEM images of fracture surfaces of tensile samples: (a) T0 alloy; (b) T1 alloy; ($a_1$, $a_2$, $b_1$, $b_2$) Local magnification of dot frames in (a) and (b), respectively (1−Dimple; 2−Cleavage plane; 3−Tearing ridge; 4−Crack; 5−Particle; 6−Fractured particle)

and few dimples are observed on the fracture surface, indicating a quasi-cleavage fracture mode. In the local magnification of dot frames in Fig. 10(a), it can be clearly seen that many cracks are created on the $Mn_5Si_3$ particles with hollows, and the prism-like particles are seriously fractured along the cross and longitudinal sections. Considering the lowest binding force of close-packed faces, the cleavage fracture surfaces of $Mn_5Si_3$ particles should be (0002) and $(10\bar{1}0)$ planes, respectively. With the MS-PMF treatment, a lot of small and deep dimples are dominant features and a ductile failure mode can be determined for the T1 alloy, as shown in Fig. 10(b). The cracked $Mn_5Si_3$ particles are rarely observed on the fracture surface and there are obvious pull-out marks of particles at the bottom of some dimples (Figs. 10($b_1$) and ($b_2$)).

It can be found that the $Mn_5Si_3$ particles with and without hollows present different failure types during the tensile test, and the influence on the fracture mechanism of brass alloys is shown in Fig. 11. Under uniaxial tension the stress efficiently transfers from the matrix to $Mn_5Si_3$ particles, especially at the locations of geometric defects [18]. In the T0 alloy, some particles with hollows are prone to fracture along different close-packed faces to form the cleavage planes with cracks, due to the higher stress concentration combined with significantly reduced fracture strength according to the Griffith theory [19]. Under lower external stress, the expansion of cleavage surfaces and connection of cracks eventually lead to the macrofracture of the material. For the T1 alloy, the matrix yields larger plastic deformation under higher stress while few particles are debonded from the matrix with microvoids left. The microvoids continuously emerge until the macroscopic fracture takes place. Therefore, both the tensile failure strength and ductility of brass alloy are effectively improved after the MS-PMF treatment.

Many investigations [4,6] have indicated that the major strengthening effect of the $Mn_5Si_3$ reinforced brass is matrix/particle load transfer

strengthening. To quantitatively study the influence of $Mn_5Si_3$ phase morphology on the strengthening contribution, finite element analysis (FEA) method is used to simulate the uniaxial tensile deformation of T0 and T1 alloys via Abaqus software. Figure 12 shows the generated 2D geometrical models with mesh grids and boundary conditions. To ensure the accuracy of the simulation, dozens of particles are included in the model. The particles distribute randomly in the plane and do not overlap each other. The volume fraction and dimension of $Mn_5Si_3$ particles (including center hollow) are set according to the microstructure observation. Ten SEM images and hundreds of particles were analyzed statistically, and the mean values of volume fraction and dimension were obtained. To simplify the calculation, a forged Cu−35Zn−3Al alloy was prepared approximately as the matrix alloy. Detailed parameters of the geometric models, and the properties of matrix alloy and $Mn_5Si_3$ phase are displayed in Table 2. It should be noted that the matrix strength is optimized based on the experimental values, in combination with fine grain strengthening and thermal mismatch strengthening produced by $Mn_5Si_3$ particles. The specific calculation process is shown in the Supplementary Information.

In this simulation, the matrix and $Mn_5Si_3$

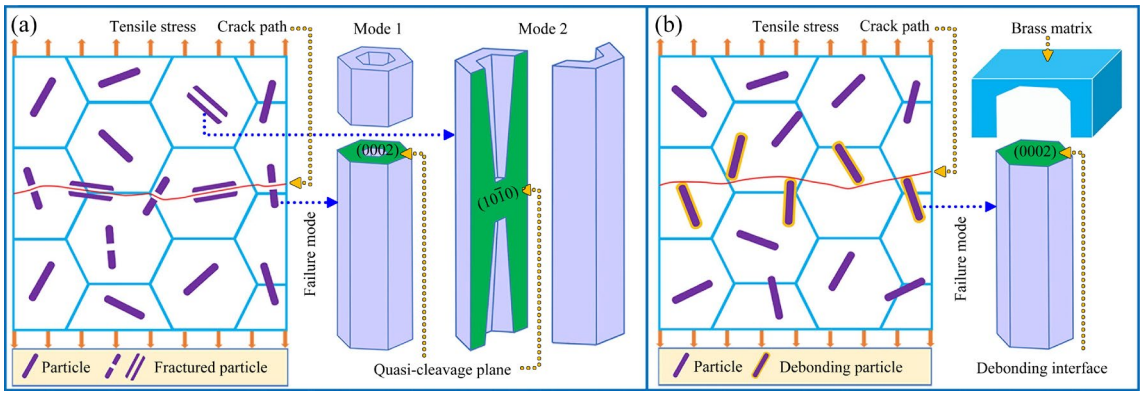


**Fig. 11** Schematic diagram illustrating tensile fracture mechanism of alloys and failure mechanism of $Mn_5Si_3$ phase: (a) T0 alloy; (b) T1 alloy

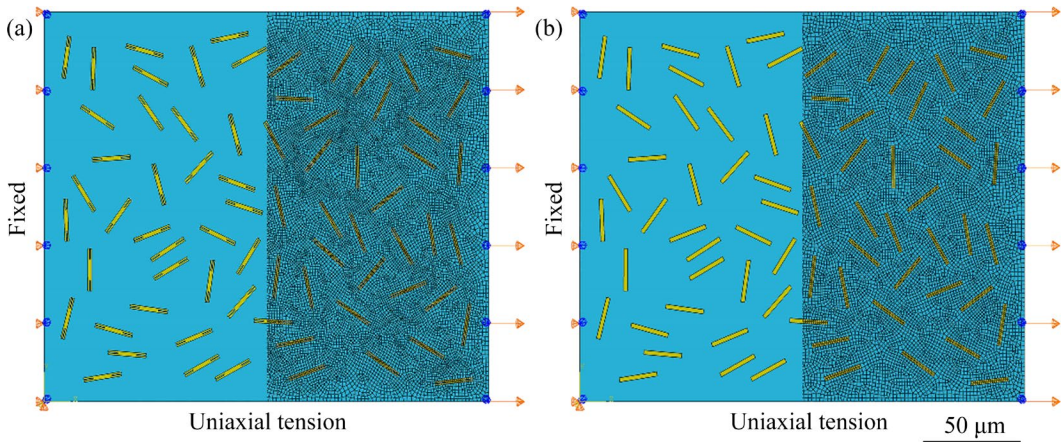


**Fig. 12** Generated 2D geometrical models with mesh grids and boundary condition of T0 alloy (a) and T1 alloy (b) for FEA

**Table 2** Parameters of geometric models and properties of matrix alloy (Cu−35Zn−3Al) and $Mn_5Si_3$ phase

| Material | Volume fraction/% | Dimension/μm | Young's modulus/GPa | Poisson's ratio | Yield strength/MPa | Tensile strength/MPa |
|---|---|---|---|---|---|---|
| Matrix alloy | 93.5 | 230×180 | 95 | 0.32 | 280 | 483 |
| $Mn_5Si_3$ | 6.5 | 18×2 (4.5×0.5) | 217 | 0.24 | – | – |

particles undergo elastoplastic and elastic deformation respectively. A ductile damage model is used for the matrix with the fracture strain of 0.2. A brittle fracture model is adopted for the $Mn_5Si_3$ particles with hollows in the T0 alloy due to the serious cleavage fracture during tension. For a brittle compound, generally the fracture strength of $\sigma$ is less than $E/100$, where $E$ is the elastic modulus. Thus, the fracture stress of $Mn_5Si_3$ particles with hollows is about 2170 MPa and the fracture strain is about 0.01. Figure 13(a) shows the simulated stress–strain curves of T0 and T1 alloys. Stress and strain values of the whole model during tensile deformation are calculated by averaging the values of all grid nodes. The time nodes of particle fracture initiation and reaching critical failure condition are shown by the arrows. Table 3 lists the comparison between the simulated and experimental results of T0 and T1 alloys. The calculated elastic modulus of the FEA models is close to the test value of alloys, which indicates good model rationality. The simulated strength and elongation are in good agreement with the measurement. Hence, the reduced load transfer strengthening resulted by the fracture damage of $Mn_5Si_3$ particles is the main reason for the decrease in strength and ductility of T0 alloy. In addition, there are some difference between the simulation and experimental results, which may be related to many aspects, such as ignoring the interface cracking of particles and solution strengthening of residual Mn and Si elements, and the modeling accuracy.

To evaluate the load transfer capacity of $Mn_5Si_3$ particles with and without hollows, the stress partition parameter ($R_{m/p}$) between the matrix and particles is used, which can be expressed by [20]

$$R_{m/p}=\frac{\sigma_{matrix}}{\sigma_{particle}} \tag{2}$$

where $\sigma_{matrix}$ and $\sigma_{particle}$ are the average stresses on the matrix and particles, respectively. Figure 13(b) displays the variation curves of $R_{m/p}$ as a function of strain for T0 and T1 alloys. In the stage of lower strain with $\varepsilon<0.02$, the curves gradually decline and the stress is continuously transferred from the matrix to $Mn_5Si_3$ particles. $R_{m/p}$ of T0 alloy is slightly lower than that of T1 alloy, which means that more stress is concentrated on the particles with hollows. In the stage of plastic deformation with $\varepsilon>0.02$, $R_{m/p}$ of T1 alloy slowly decreases and then remains a sight change. $R_{m/p}$ of T0 alloy gradually increases and becomes greater than that of T1 alloy, which is ascribed to the fracture damage of some particles, resulting in the reduction of stress transfer capacity.

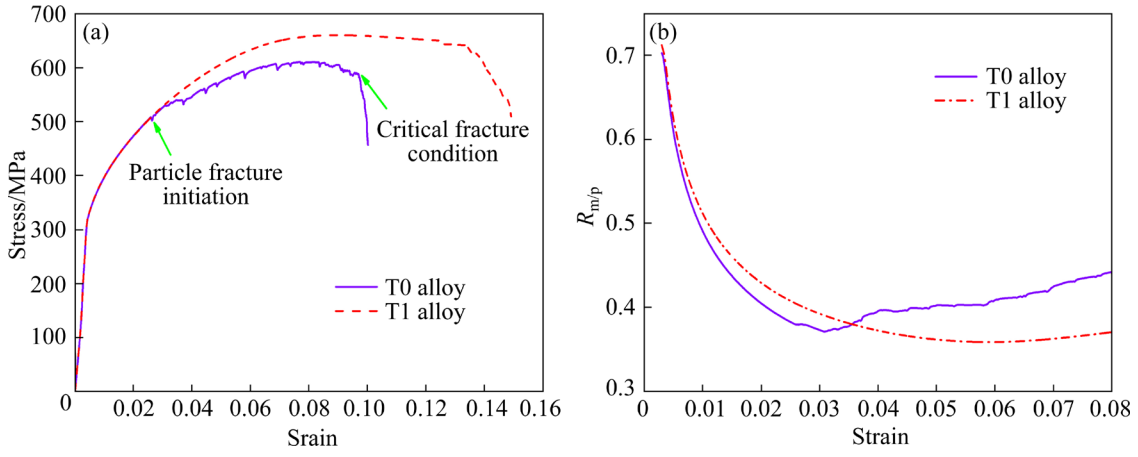


**Fig. 13** Simulated stress–strain curves (a) and stress partition parameter ($R_{m/p}$) between matrix and $Mn_5Si_3$ phase (b) of T0 and T1 alloys

**Table 3** Comparison between simulated and experimental results of mechanical properties of T0 and T1 alloys

| Alloy | Elastic modulus/GPa | | Yield strength/MPa | | Tensile strength/MPa | | Elongation/% | |
|---|---|---|---|---|---|---|---|---|
| | Simulated | Experimental | Simulated | Experimental | Simulated | Experimental | Simulated | Experimental |
| T0 | 63 | 61 | 318 | 310 | 609 | 601 | 10.0 | 9.2 |
| T1 | | | 318 | 314 | 660 | 655 | 14.9 | 15.3 |

Figures 14(a−d) show the von Mises stress contours of T0 and T1 alloys at different strain conditions. With increasing the strain, the stress on the particles gradually increases, and higher level of stress i.e. the stress concentration, exists on some particles. The stress concentration degree on the particles of T0 alloy is higher than that of T1 alloy, especially at the hollow locations, as shown by the arrows in the enlarged view of particles (Figs. 14($a_1$−$d_2$)). Correspondingly, the strain contours of particles at the same model strain are displayed in Figs. 14(e, f). It can be seen that the particles subjected to higher stress also exhibit greater strain concentration (Figs. 14($e_1$, $e_2$)). Therefore, brittle fracture is more likely to occur on the $Mn_5Si_3$ particles with hollows, which remarkably reduces the load transfer strengthening in the T0 alloy.

### 3.4 Effect of $Mn_5Si_3$ morphology on wear resistance

Figure 15(a) shows the variation curves of wear loss as a function of sliding distance for T0 and T1 alloys. According to the change law, the friction process can be divided into two stages. In Stage I the curves rise linearly and the critical sliding distances of T0 and T1 alloys are 300 and 500 m, respectively. In Stage II the curves increase rapidly and the T1 alloy exhibits lower wear loss. The friction coefficient curves of two alloys with sliding distance are displayed in Fig. 15(b). During the steady-state wear, the T0 alloy presents higher average friction coefficient with violent fluctuation, which is proven by a greater standard deviation ($\sigma$).

Figure 16 shows different wear features of samples after sliding 400 m. The main wear forms can be determined as adhesive wear and abrasive wear, according to the observation of grooves and plastic deformation on the worn surfaces, strip-like wear debris, and material transfer on the counterpart surfaces (Figs. 16(a, d)) [21,22]. Oxidative wear is confirmed by detecting the O element distribution on the wear surfaces [23]. Compared with T1 alloy,

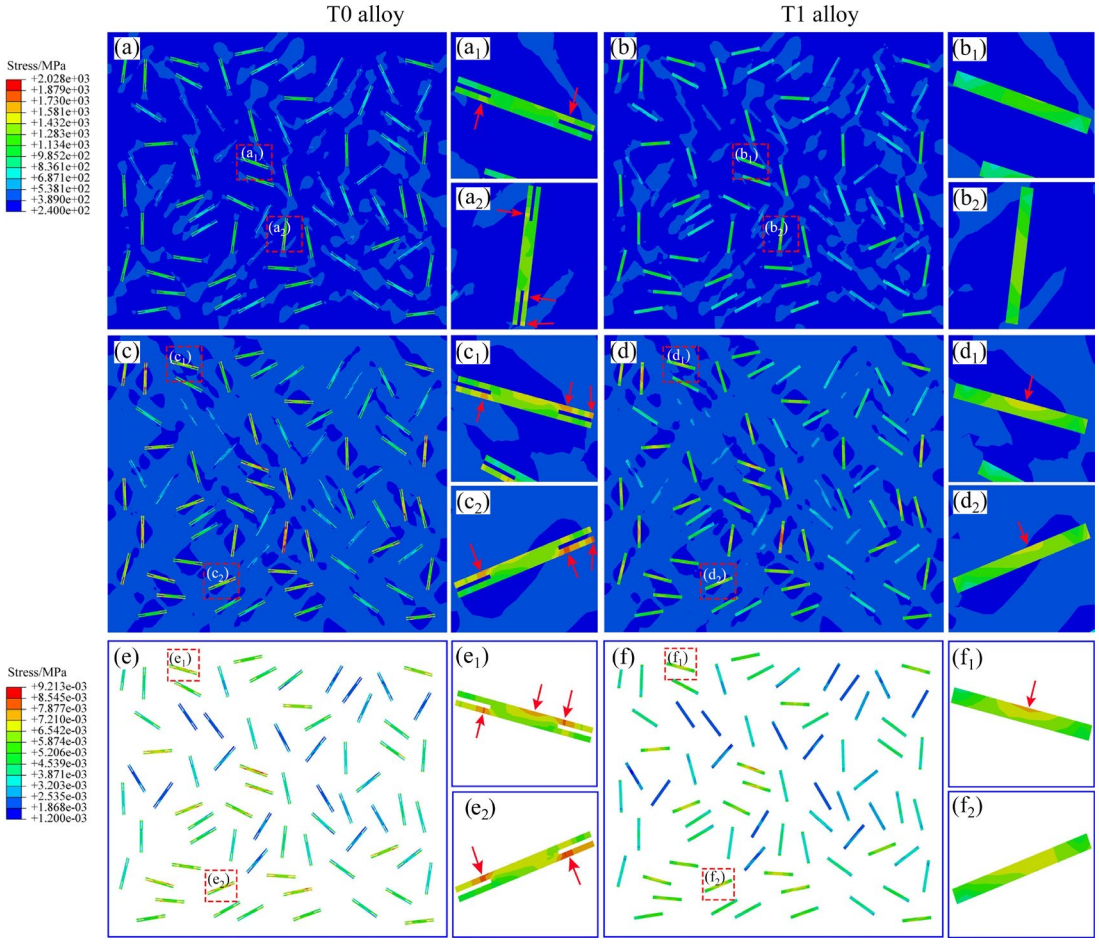


**Fig. 14** von Mises stress contours of alloys at different strains of 0.015 and 0.025: (a, c) T0 alloy, (b, d) T1 alloy; strain contours of $Mn_5Si_3$ particles at strain of 0.025; (e) T0 alloy; (f) T1 alloy; ($a_1$−$f_1$, $a_2$−$f_2$) Enlarged views of stress and strain distribution within $Mn_5Si_3$ particles

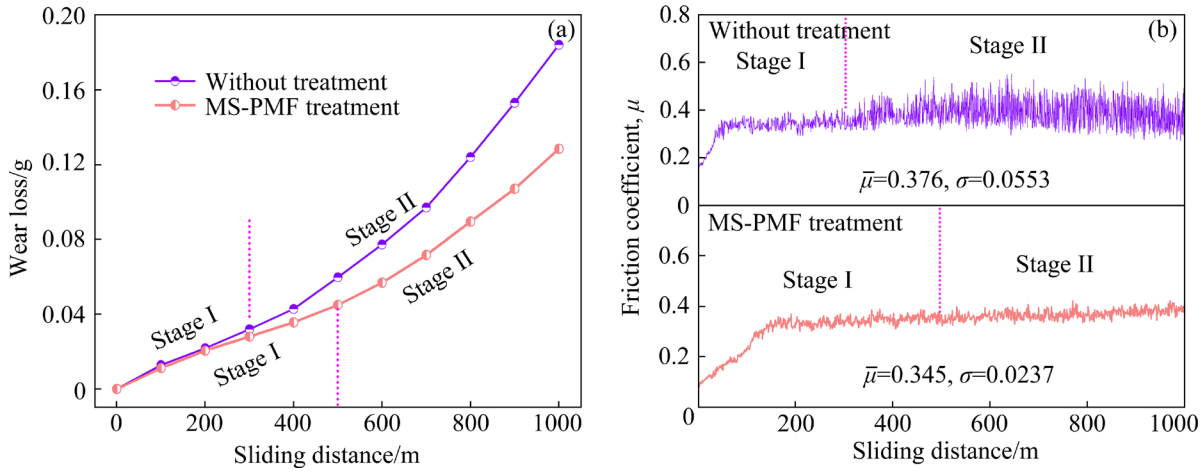


**Fig. 15** Wear loss (a) and friction coefficient (b) as function of sliding distance for alloys without and with MS-PMF treatment

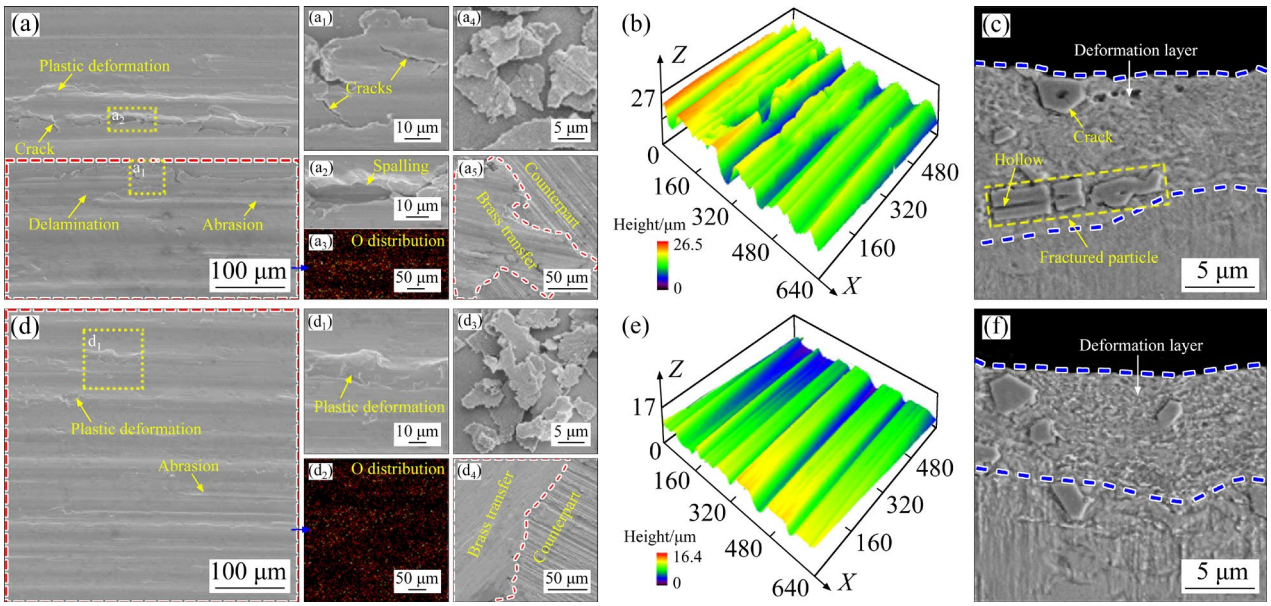


**Fig. 16** SEM micrographs and 3D images of worn surfaces and subsurface microstructures showing wear features of alloy samples after sliding 400 m: (a−c) T0 alloy; (d−f) T1 alloy; ($a_1$, $a_2$, $d_1$) Local magnification of dot frames in (a) and (d); ($a_3$, $d_2$) EDS maps of dashed frame showing O element distribution; ($a_4$, $d_3$) Wear debris; ($a_5$, $d_4$) SEM micrographs of worn surfaces of counterpart steel

small amounts of cracks and spallings can be clearly seen on the worn surface of T0 alloy, as shown in the local magnification of dot frames (Figs. 16($a_1$, $a_2$)). This suggests the occurrence of delamination wear, which is also demonstrated by the 3D wear topography (Fig. 16(b)). In addition, the continuous deformation layer is formed below the wear surfaces (Figs. 16(c, f)). For T0 alloy, cracks appear on the particles with hollows in the worn subsurface while a few particles are broken into several fragments (Fig. 16(c)), which forms the origin of surface spallings. Archard model and Rabinowicz model can be respectively used to describe the wear volume of adhesion and abrasion, which is proportional to the sliding distance and inversely proportional to the hardness of materials [24,25]. Therefore, during the first-stage friction, T0 and T1 alloys exhibit little difference in wear loss due to the similar yield strength and hardness. Delamination occurs earlier during friction of the T0 alloy, since the accumulated plastic deformation under short-distance sliding can

lead to the subsurface originated cracking and spallings [26,27].

Figure 17 shows different wear features of alloys after sliding a total of 1000 m. It is found that delamination has become one of the dominant wear forms alongside adhesive and abrasive wear. The T0 alloy presents heavier delamination indicated by lots of severe spallings on the worn surfaces (Fig. 17(a)), propagation of longer surface cracks (Fig. 17($a_1$)), and thicker wear debris with serious cracking (Fig. 17($a_2$)). The obvious relief of 3D wear topography of the T0 alloy exhibits a rough worn surface (Fig. 17(b)). The depth profiles of complete wear tracks for T0 and T1 alloys are displayed in Figs. 17(d, h), respectively. To quantitatively describe the fluctuation amplitude of the surface profile, the term $\lambda$ is introduced and can be calculated as follows [28]:

$$\lambda=\sum_{i=0}^{l_{max}/\Delta l}\left(d_{l=i*\Delta l}-\bar{d}\right)^2 \tag{3}$$

where $\bar{d}$ is the average depth of surface profile, $l_{max}$ is 4800 μm, $\Delta l$ is 0.625 μm, and $d_{l=i*\Delta l}$ is each measured $d$-value which corresponds to a specific $l$-value. The calculated results show that $\lambda$ of the worn surface of T0 alloy (105741 $\mu m^2$) is about 3.3 times higher than that of T1 alloy (31765 $\mu m^2$), and the relevant $d_{max}$ values are 23.2 and 9.5 μm,

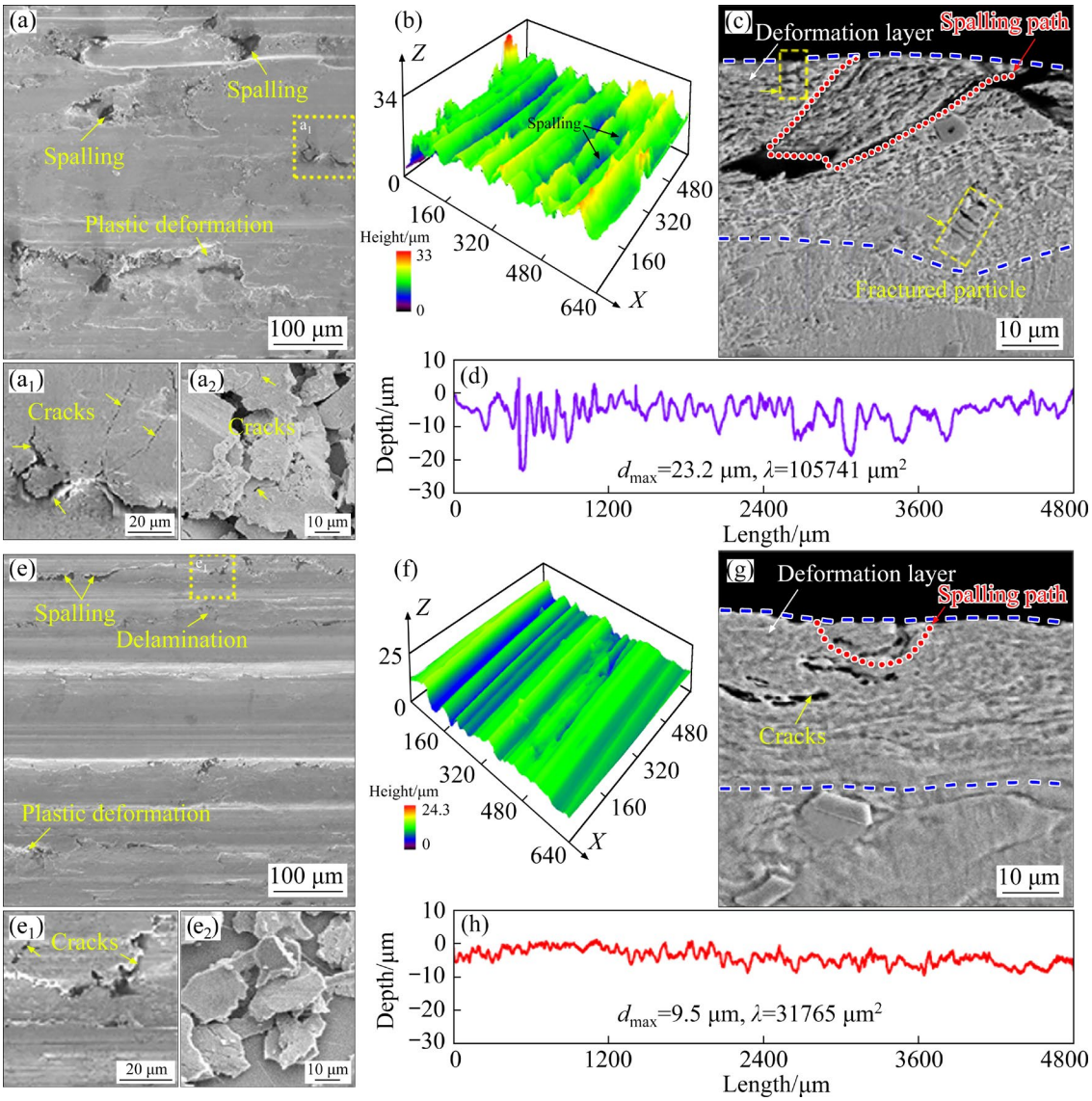


**Fig. 17** SEM micrographs, 3D images and depth profiles of worn surfaces and subsurface microstructures showing wear features of alloys after sliding total 1000 m: (a−d) T0 alloy; (e−h) T1 alloy; ($a_1$, $e_1$) Local magnification of dot frame in (a) and (e), respectively; ($a_2$, $e_2$) Wear debris

respectively. This indicates the evidently reduced wear damage with a flatter worn surface of T1 alloy. Figures 17(c) and (g) display the worn subsurface microstructures of T0 and T1 alloys with a thicker deformation layer, respectively. For the T0 alloy, severe fracture occurs on many particles with hollows, and propagation and penetration of elongated cracks are generated, resulting in the imminent spalling failure of coarse wear particle (Fig. 17(c)). In the worn subsurface of T1 alloy, the cracks are found to be developed only through the matrix in the deformation layer, and the spalling of a small piece of material is to be produced (Fig. 17(g)). The $Mn_5Si_3$ particles as hard phase favors the friction coefficient decrease of the alloy during friction. The spalling of $Mn_5Si_3$ phase reduces its real contact area with counterpart, resulting in a higher friction coefficient with larger fluctuation. Therefore, during the second-stage friction, the wear loss and friction coefficient of the T1 alloy are apparently decreased due to the reduced delamination, which is mainly ascribed to the alleviation of subsurface originated cracks and spallings.

To better understand the crack initiation conditions in the worn subsurface of alloy samples, the stress distribution below the wear surfaces is investigated. During friction the wear samples contact with counterpart surface in the form of micro-convex. The stress state at a point at the depth is complex and multiaxial, which can be described according to the Hertzian contact theory [29]. Based on the observed debris size, the micro-convex is assumed to be a hemispherical model with a radius ($r$) of 100 μm. The maximum compressive stress ($P_{max}$) on the micro-convex can be expressed as $3F/(2\pi r^2)$. The applied load $F$ is 180 N and the $P_{max}$ is calculated to be about $8.6\times10^3$ MPa. There is a three-dimensional compressive stress near the surface below the micro-convex and cracks are not easily formed. In the subsurface layers adjacent to the micro-convex, the tensile stress and shear stress exist synchronously and the cracks are most often originated in the region of maximum shear stress [30]. The $\tau_{max}$ value in the subsurface regions is about $0.25P_{max}$ and can be estimated as 2150 MPa. For the T0 alloy, the critical fracture stress $\sigma_f$ of $Mn_5Si_3$ particles along the hollow section could be expressed according to the Griffith formula [19]:

$$\sigma_f = \left(\frac{2E\gamma}{\pi a}\right)^{1/2} \quad (4)$$

where $E$(=217 GPa) is the elastic modulus, $\gamma$(≈1 J/m$^2$) is the fracture surface energy, and $a$ represents the hollow radius about 0.25 μm. Then, the $\sigma_f$ for $Mn_5Si_3$ particles with hollows is estimated as 743 MPa. The shear fracture strength of $\beta$ matrix is 0.6−0.8 times of tensile strength and calculated as 290−386 MPa. Thus, during the sliding friction of T0 alloy, cracking will occur on both the particles and matrix located in the subsurface suffering high shear stress. According to the aforementioned discussion, higher stress concentration produced on the particles with hollows will further promote the crack initiation. For the T1 alloy, the fracture strength of particles without hollows (>2170 MPa) is greater than the maximum shear stress and hardly any particles are cracked in the worn subsurface.

Therefore, the cracking of $Mn_5Si_3$ particles below the wear surface of alloy samples is very sensitive to the hollow morphology. The schematic illustrating the formation mechanism of cracks and spallings on the worn subsurfaces is displayed in Fig. 18. During friction of the T0 alloy, cracks initiate at the hollow locations of subsurface particles where being stress concentrated. Under the action of accumulated plastic deformation, severe shear fracture occurs on numerous subsurface particles with hollows. Connection of cracks between the particles and matrix leads to rapid crack growth (Fig. 18(a)). Thereafter, the long cracks propagate and penetrate up toward the surface, finally resulting in the massive spallings of bulk surface material (Fig. 18(b)). For the T1 alloy, the crack development along the ductile matrix in subsurface is limited and few spallings of small wear particle are created (Figs. 18(c, d)). In addition, the hard $Mn_5Si_3$ particles play a vital role of supporting the matrix during friction, and the broken particles will debilitate the capacity of surface material to resist the plastic deformation and microplowing. To sum up, after the MS-PMF treatment, the wear damage of adhesion and abrasion is reduced together with the mitigated delamination, and the wear resistance of brass alloy is significantly improved.

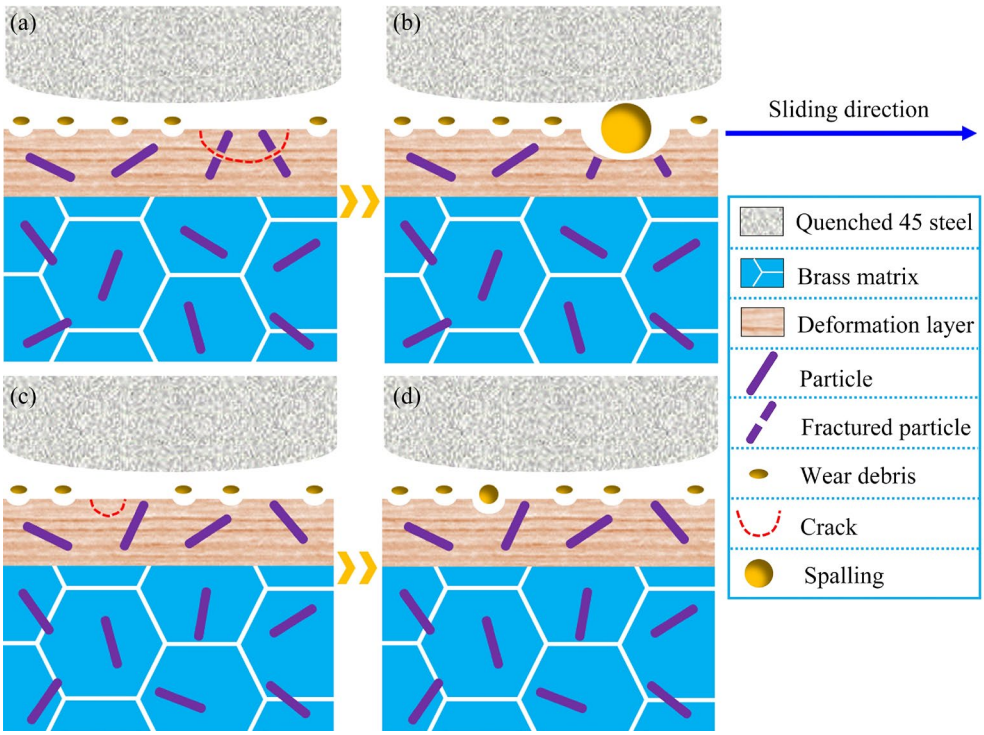


**Fig. 18** Schematic illustration of crack and spalling formation on worn subsurfaces of alloys without and with MS-PMF treatment: (a, b) T0 alloy; (c, d) T1 alloy

## 4 Conclusions

(1) The formation of hollows in the center of $Mn_5Si_3$ phase with the growth pattern of hexagonal prism is inhibited, due to the uniform solute distribution and enhanced solute diffusion through forced convection in melt, which promotes the adsorption kinetics on the prism planes and thereby hinders the generation of melt regions depleted of Mn and Si solutes in the prism center, i.e., the origin of hollows.

(2) The brass alloy achieves high tensile strength of 655 MPa and high elongation of 15.3% with great increments of 9.0% and 66.5%, respectively. The failure type of $Mn_5Si_3$ particles during tensile deformation transfers from brittle cleavage fracture to pulling out of the matrix ascribed to the higher fracture strength with diminished stress concentration. This leads to the increased particle/matrix load transfer strengthening, favored by the good agreement between finite element simulation and experimental results.

(3) The wear resistance of brass alloy is significantly improved because of the reduced delamination wear, since the severe shear fracture on the $Mn_5Si_3$ particles with hollows under friction induced shear plastic deformation is restrained, thus alleviating the subsurface originated crack propagation and spallings.

### CRediT authorship contribution statement

**Hang LI:** Conceptualization, Methodology, Writing – Original draft preparation, Writing – Review & editing, Funding acquisition; **Dong-tao NIU:** Visualization, Investigation; **Zhong-tao ZHANG:** Formal analysis; **Fan YANG:** Data curation; **Hong-xia WANG:** Formal analysis; **Wei-li CHENG:** Writing – Review & editing, Funding acquisition.

### Declaration of competing interest

The authors declare that they have no known competing financial interests or personal relationships that could have appeared to influence the work reported in this paper.

### Acknowledgments

The authors gratefully acknowledge the supports of the National Natural Science Foundation of China (No. 51901153), and Natural Science Foundation of Shanxi Province, China (No. 201901D211096).

## Supplementary Information

Supplementary Information in this paper can be found at: http://tnmsc.csu.edu.cn/download/15-p0918-2022-0965-Supplemetary_Information.pdf.

## References


[1] LI Hang, JIE Jin-chuan, ZHANG Peng-chao, JIA Chun-xu, WANG Tong-min, LI Ting-ju. Study on the formation and precipitation mechanism of $Mn_5Si_3$ phase in the MBA-2 brass alloy [J]. Metallurgical and Materials Transactions A, 2016, 47: 2616−2624.

[2] GOU Pei-pei, NIU Ben, WANG Na, DONG Zhi-gang, LI Zhen, WANG Qing, KANG Ren-ke, DONG Chuang. Composition-optimized Cu−Zn−(Mn,Fe,Si) alloy and its microstructural evolution with thermomechanical treatments [J]. Journal of Materials Engineering and Performance, 2021, 31: 590−601.

[3] MINDIVAN H, ÇIMENOĞLU H, KAYALI E S. Microstructures and wear properties of brass synchroniser rings [J]. Wear, 2003, 254: 532−537.

[4] LI Hang, JIE Jin-chuan, LIU Shi-chao, ZHANG Yu-bo, LI Ting-ju. Crystal growth and morphology evolution of D88 $(Mn,Fe)_5Si_3$ phase and its influence on the mechanical and wear properties of brasses [J]. Materials Science and Engineering: A, 2017, 704: 45−56.

[5] BIE Li-fu, CHEN Xiao-hong, LIU Ping, ZHANG Tao, XU Xiang-liu. Morphology evolution of $Mn_5Si_3$ phase and effect of Mn content on wear resistance of special brass [J]. Metals and Materials International, 2019, 26: 431−443.

[6] CHEN Shao-hua, MI Xu-jun, HUANG Guo-jie, LI Yan-feng. Effect of Ce addition on microstructure and properties of Cu−Zn−Mn−Al-based alloy [J]. Materials Research Express, 2018, 6: 016518.

[7] LIN Y H, CHUANG W S, HUANG J C, CHAO C Y, CHANG C M. Influence from size and morphology of $Mn_5Si_3$ on wear resistance of Cu−Zn−Al−Mn−Si alloys [J]. Metallurgical and Materials Transactions A, 2019, 50: 3148−3157.

[8] MANANI S, PRADHAN A K. Effects of melt thermal treatment on cast Al−Si alloys: A review [J]. Materials Today: Proceedings, 2022, 62: 6568−6572.

[9] ZHA Min, WANG Hui-yuan, LIU Bo, ZHAO Bing, LIANG Min-li, LI Dong, JIANG Qi-chuan. Influence of melt superheating on microstructures of Mg−3.5Si−1Al alloys [J]. Transactions of Nonferrous Metals Society of China, 2008, 18(Suppl.): S107−S112.

[10] XU C L, JIANG Q C. Morphologies of primary silicon in hypereutectic Al−Si alloys with melt overheating temperature and cooling rate [J]. Materials Science and Engineering: A, 2006, 437: 451−455.

[11] ECKERT S, NIKRITYUK P A, WILLERS B, RÄBIGER D, SHEVCHENKO N, NEUMANN-HEYME H, TRAVNIKOV V, ODENBACH S, VOIGT A, ECKERT K. Electromagnetic melt flow control during solidification of metallic alloys [J]. The European Physical Journal Special Topics, 2013, 220: 123−137.

[12] LI Ying-ju, MA Xiao-ping, YANG Yuan-sheng. Grain refinement of as-cast superalloy IN718 under action of low voltage pulsed magnetic field [J]. Transactions of Nonferrous Metals Society of China, 2011, 21: 1277−1282.

[13] ZHANG L, ZHOU W, HU P H, ZHOU Q. Microstructural characteristics and mechanical properties of Mg–Zn–Y alloy containing icosahedral quasicrystals phase treated by pulsed magnetic field [J]. Journal of Alloys and Compounds, 2016, 688: 868−874.

[14] SUNAGAWA I. Crystals: growth, morphology, and perfection [M]. Cambridge: Cambridge University Press, 2005.

[15] SMITHELLS C J, GALE W F, TOTEMEIER T C. Smithells metals reference book [M]. Amsterdam: Elsevier Butterworth–Heinemann, 2004.

[16] HARTMAN P. Crystal growth: An introduction [M]. Amsterdam: North-Holland Pub. Co., 1973.

[17] GRIFFITHS D J. Introduction to electrodynamics [M]. NJ: Prentice Hall, 1999.

[18] LIN Gao-yong, LI Kun, FENG Di, FENG Yong-ping, SONG Wei-yuan, XIAO Meng-qiong. Effects of La−Ce addition on microstructure and mechanical properties of Al−18Si−4Cu−0.5Mg alloy [J]. Transactions of Nonferrous Metals Society of China, 2019, 29: 1592−1600.

[19] XU C L, WANG H Y, YANG Y F, JIANG Q C. Effect of Al−P−Ti−TiC−$Nd_2O_3$ modifier on the microstructure and mechanical properties of hypereutectic Al−20wt.%Si alloy [J]. Materials Science and Engineering: A, 2007, 452/453: 341−346.

[20] ZHANG J F, ANDRÄ H, ZHANG X X, WANG Q Z, XIAO B L, MA Z Y. An enhanced finite element model considering multi strengthening and damage mechanisms in particle reinforced metal matrix composites [J]. Composite Structures, 2019, 226: 111281.

[21] HU Zhao-hua, WU Guo-hua, XU Jia, MO Wen-fei, LI Yan-lei, LIU Wen-cai, ZHANG Liang, DING Wen-jiang, QUAN Jonathan, CHANG Yuan-wei. Dry wear behavior of rheo-casting Al−16Si−4Cu−0.5Mg alloy [J]. Transactions of Nonferrous Metals Society of China, 2016, 26: 2818−2829.

[22] YANG Yang, LIANG Lu-xin, WU Hong, LIU Bo-wei, QU Hui, FANG Qi-hong. Effect of zinc powder content on tribological behaviors of brake friction materials [J]. Transactions of Nonferrous Metals Society of China, 2020, 30: 3078−3092.

[23] KONG X L, LIU Y B, QIAO L J. Dry sliding tribological behaviors of nanocrystalline Cu−Zn surface layer after annealing in air [J]. Wear, 2004, 256: 747−753.

[24] ARCHARD J F. Contact and rubbing of flat surfaces [J]. Journal of Applied Physics, 1953, 24: 981−988.

[25] RABINOWICZ E. Friction and wear of materials [M]. New York: John Wiley & Sons Inc, 1995.

[26] MOAZAMI-GOUDARZI G M, NEMATI A. Tribological behavior of self lubricating Cu/$MoS_2$ composites fabricated by powder metallurgy [J]. Transactions of Nonferrous Metals Society of China, 2018, 28: 946−956.

[27] SUN Yang, WANG Yan, LI Yun, ZHOU Ke-chao, ZHANG Lei. Tribological behaviors of Ag−graphite composites reinforced with spherical graphite [J]. Transactions of Nonferrous Metals Society of China, 2020, 30: 2177−2187.

[28] WANG Xian-long, JIE Jin-chuan, LIU Shi-chao, DONG Zhuang-zhuang, YIN Guo-mao, LI Ting-ju. Growth mechanism of primary $Ti_5Si_3$ phases in special brasses and their effect on wear resistance [J]. Journal of Materials Science & Technology, 2021, 61: 138−146.

[29] JOHNSON K L. Contact mechanics [M]. Cambridge: Cambridge University Press, 1987.

[30] SADEGHI F, JALALAHMADI B, SLACK T S, RAJE N, ARAKERE N K. A review of rolling contact fatigue [J]. Journal of Tribology, 2009, 131: 041403.

# 熔体过热和脉冲磁场协同处理对 $Mn_5Si_3$ 增强 Cu−35Zn−3Al 合金显微组织、力学和耐磨性能的影响

李 航[1,2]，牛冬涛[1]，张忠涛[2]，杨 帆[1]，王红霞[1]，程伟丽[1]

1. 太原理工大学 材料科学与工程学院，太原 030024；
2. 金龙精密铜管有限公司，重庆 404100

**摘 要：**研究熔体过热和脉冲磁场协同处理对 $Mn_5Si_3$ 增强 Cu−35Zn−3Al 合金显微组织、力学和耐磨性能的影响。研究结果表明，协同处理促进了熔体中的溶质迁移以及 $Mn_5Si_3$ 晶体生长的吸附动力学，抑制了六棱柱形貌 $Mn_5Si_3$ 颗粒上孔洞的形成。协同处理后热锻态合金的抗拉强度和伸长率分别提高了 9.0%和 66.5%，这是由于拉伸变形过程中不含孔洞的 $Mn_5Si_3$ 颗粒断裂强度提高，产生的应力集中减小，因此失效方式由脆性解理断裂转变为从基体中拔出，颗粒和基体间的载荷传递作用增强。在承受摩擦时，协同处理后合金的磨损亚表层中 $Mn_5Si_3$ 颗粒不易发生剪切断裂，抑制了裂纹扩展和材料剥落，因而产生的剥层磨损减小，合金耐磨性显著提高。

**关键词：**复杂黄铜；$Mn_5Si_3$ 相；脉冲磁场；强化机理；耐磨性

**(Edited by Xiang-qun LI)**